batteries

MDPI

Article

Symmetric Supercapacitor Based on Nitrogen-Doped and Plasma-Functionalized 3D Graphene

Kavitha Mulackampilly Joseph [1] and Vesselin Shanov [1,2,*]

[1] Department of Mechanical and Materials Engineering, University of Cincinnati, Cincinnati, OH 45221, USA
[2] Department of Chemical and Environmental Engineering, University of Cincinnati, Cincinnati, OH 45221, USA
* Correspondence: vesselin.shanov@uc.edu

Abstract: Nitrogen-doped, 3-dimensional graphene (N3DG), synthesized as a one-step thermal CVD process, was further functionalized with atmospheric pressure oxygen plasma. Electrodes were fabricated and tested based on the functionalized N3DG. Their characterization included scanning electron microscopy (SEM), Raman spectroscopy, X-ray photoelectron spectroscopy (XPS), Brunauer–Emmet–Teller (BET), and electrochemical measurements. The tested electrodes revealed a 208% increase in the specific capacitance compared to pristine 3D graphene electrodes in a three-electrode configuration. The performed doping and plasma treatment enabled an increase in the electrode's surface area by 4 times compared to pristine samples. Furthermore, the XPS results revealed the presence of nitrogen and oxygen functional groups in the doped and functionalized material. Symmetric supercapacitors assembled from the functionalized 3D graphene using aqueous and organic electrolytes were compared for electrochemical performance. The device with ionic electrolyte $EMIMB_4$ electrolyte exhibited a superior energy density of 54 Wh/kg and power density of 1224 W/kg. It also demonstrated a high-cyclic stability of 15,000 cycles with a capacitance retention of 107%.

Keywords: energy storage; supercapacitor; nitrogen doping; oxygen functionalization; atmospheric oxygen plasma; 3-dimensional graphene; ionic electrolyte; $EMIMBF_4$

Citation: Joseph, K.M.; Shanov, V. Symmetric Supercapacitor Based on Nitrogen-Doped and Plasma-Functionalized 3D Graphene. *Batteries* **2022**, *8*, 258. https://doi.org/10.3390/batteries8120258

Academic Editor: King Jet Tseng

Received: 25 October 2022
Accepted: 21 November 2022
Published: 28 November 2022

1. Introduction

Electrochemical energy storage research has revealed a dramatic surge in recent years driven by the demand for portable high-power electronic devices and electric vehicles. Among the various energy storage devices, such as fuel cells, capacitors, and lithium-ion batteries, supercapacitors are popular due to their high power density, long cyclic stability, and energy efficiency. All these advantages enable them to be useful in applications such as pulsed laser systems, computers, interfacing of power grids, and load leveling in renewable energy generation systems [1].The charge storage mechanism in supercapacitors can be electric double-layer charging (EDLC) or pseudocapacitive type. In EDLC, the charge storage is non-Faradaic, and happens at the electrolyte–electrode interface by the separation of charge in a Helmholtz double layer, while in pseudo capacitance, charge storage is Faradaic, resulting in fast charge transfer through redox reactions [2,3]. Electrochemical supercapacitors are superior to electrostatic and electrolytic capacitors but inferior to batteries with respect to energy density. This hinders them from practical and prominent energy-efficient applications in industrial environments. Therefore, fabricating high-energy density supercapacitors is of particular interest [4,5].

The energy density of a supercapacitor is given as the product of the capacitance and square of the cell voltage. In turn, the capacitance and the cell voltage depend on the electrode and the type of electrolyte, respectively. Electrolyte engineering has been making steady progress in recent years, with research work narrowing down to tuning the

amount of electrolyte solvation [6] and the development of solvents and cyclic anions [7] for high-voltage energy storage devices. While aqueous electrolytes have a limited voltage window ($\leq$1 V), organic electrolytes exhibit a higher voltage window (2.5–2.8 V). In the case of aqueous/alkaline electrolytes, the voltage window is narrowed due to the relatively low decomposition voltage of water. However, organic electrolytes are toxic, flammable, corrosive, and volatile [8]. Recently, a new group of electrolytes called ionic liquids (ILs) has been widely used due to their wider voltage window ($\geq$ 3 V), non-flammability, and stability [9]. The ionic electrolyte structure consists of asymmetrical organic/inorganic anions and organic cations that can remain in the liquid phase below 100 °C or even at room temperature. When using neat ionic liquid electrolytes, the double-layer charging is accomplished by potential induced adsorption of electrolyte ions onto the surface of charged inert electrodes. In this case, the charge transfer occurs without the help of additional solvent media. Thus, ILs do not require voltage-limiting solvents and are safe and solvent-free, with highly ionized ions and a broad liquid temperature range. ILs can afford capacitive electro sorption at the electrolyte/electrode interface under high potential voltages [10,11]. One such electrolyte called EMIMBF4 (1-ethyl 3-methyl imidazolium tetrafluoroborate) is commonly used and can reach a working voltage as high as 3.8 V or 4 V [12], as reported by Chen et al. and Hurilechaoketu et al., respectively [13,14]. Due to their large ion sizes, these electrolytes exhibit low conductivity and high viscosity, hindering their ion diffusion in narrow pores. However, this problem can be overcome by electrodes with a hierarchical architecture and high surface area.

Carbon-based materials such as graphite, activated carbon, and carbon nanotubes are widely used as electrodes in energy storage applications and, most recently, in rechargeable batteries including potassium ion batteries [15]. Carbon nanotubes and activated carbon are also appropriate candidates for supercapacitor applications with their high surface area, thermal and chemical stability, and electrical conductivity. However, supercapacitors, based on them, lack high-power density and longevity due to non-uniform pore size distribution and the presence of surface functional groups [16]. Graphene, a 2-dimensional material made of sp^2 hybridized carbon with a honeycomb lattice structure, can be a potential candidate for supercapacitor application due to its high surface area, exceptional electrical conductivity, and mechanical stability [17,18]. Still, the major drawback of top-down/chemically synthesized 2D graphene is its tendency to restack during the 3D structure assembly due to the high surface energy that prevents ion electrolyte diffusion resulting in a diminished surface area and capacitance. A recent publication claims highly pure, crystalline, large-scale, low-cost, chemically synthesized 3D graphene for energy storage applications [19]. However, a bottom-up synthesis process such as chemical vapor deposition (CVD) is more advantageous due to (a) greater control over nucleation sites and (b) easily scalable characteristics. Although graphene is produced in our lab by other methods, such as 3D printing with CVD [20] and plasma CVD process, the thermal CVD process is preferred because of its simplicity and ease of operation. Therefore, in this work, thermal CVD process was used to make hierarchical 3-dimensional graphene which could translate 2D properties into the 3D structure.

Doping graphene with nitrogen is a proven strategy to fine-tune the electronic properties of graphene. Compared to the pristine material, nitrogen-doped graphene consists of activated regions in the graphene lattice created by the change in spin density and charge distribution of carbon atoms. Nitrogen doping not only increases the electron density but also induces functional groups, thus increasing the electrical conductivity besides capacitive property and facilitating fast charge–discharge of the supercapacitors [21–24]. In this work, N-doped (nitrogen-doped) graphene is synthesized by a CVD process using methane as a precursor and acetonitrile as a nitrogen dopant. The high-temperature synthesis (1000 °C) imparts a stable graphitic structure in graphene with lower-than-expected nitrogen content. The low nitrogen content could be due to a high reaction temperature [25].

To further modify the graphene structure for better capacitive properties, atmospheric pressure oxygen plasma treatment was employed. Our recently published review pa-

per [26] lists the advantages of atmospheric plasma treatment as a strategy to improve the electrode performance in supercapacitors. In brief, oxygen plasma treatment (a) increases the surface area by opening new pores and modifying the pore structure, (b) creates new functional groups, and (c) changes the surface energy to increase the hydrophilicity. Compared to wet oxygen functionalization methods, atmospheric pressure oxygen plasma treatment is much simpler and eco-friendly. Wet chemical methods often require multiple steps with strong chemicals to attain the required functionality effects and can alter the bulk chemical structure of the treated nanocarbons. Our group has previously reported the advantages of plasma functionalization in increasing wettability and enhancing the material's electrochemical properties [27–29].

This work employs a systematic approach to fabricating supercapacitors with high capacitance, energy density, and long cyclic stability. Hence, all the strategies mentioned above to increase the energy density and cycle life of the device are combined in the following sequence: (1) synthesizing a highly stable graphitic structured graphene with nitrogen functional group by a CVD process; (2) functionalizing the N-doped graphene with atmospheric pressure oxygen plasma to enhance the capacitive property; and (3) fabricating a symmetric supercapacitor with the made electrodes using ionic electrolyte (operating voltage of 3 V) to obtain a device with satisfactory energy and power densities. As shown later, the symmetric supercapacitor fabricated with the strategies mentioned above revealed superior electrochemical performance compared to pristine graphene-based supercapacitors.

2. Materials and Methods

2.1. Materials

Polystyrene (21,000 Mw), plasticizer di-(ethylene glycol) dibenzoate (DEGD) (TCI SG 1.18), toluene (Sigma Aldrich, Milwaukee, WI, USA), and nickel powder (Alfa Aesar, Tewksbury, MA, USA) 3–7 μm particle size and 1.8–2.7 g/cm^3 apparent density), acetonitrile (99.0%), ionic liquid EMIMBF4 (99.0%), was obtained from Sigma-Aldrich Co Ltd. All the chemicals were used as received. The gases used in the CVD process (H_2, CH_4, Ar (Liquified), and atmospheric plasma (O_2 and He) were of UHP (ultra-high-pure) grade procured from the Wright Brothers, Cincinnati, OH, USA.

2.2. Synthesis of Nitrogen-Doped 3-Dimensional Graphene

Pristine three-dimensional graphene (P3DG) was synthesized via a Chemical Vapor Deposition (CVD) process as described in our publication elsewhere [30]. The process was slightly modified to synthesize nitrogen-doped three-dimensional graphene (N3DG), wherein acetonitrile is used as nitrogen dopant [31]. Nickel was used as a catalyst substrate for graphene synthesis. The Ni-catalyst slurry was prepared by mixing 5.5 g of the polymer polystyrene as the binder with 1.75 mL of the plasticizer diethylene glycol dibenzoate, 40 mL toluene, and 40 g nickel powder, followed by knife casting. Then, the air-dried Ni-polymer catalyst was placed in the CVD reactor employing the following parameters. First, the sample was heated by a pre-programmed temperature ramp at a rate of 25 °C/min for approximately 40 min until it reached 1000 °C, in the presence of argon (1000 sccm) and hydrogen (325 sccm). This temperature was further held for 5 min which enabled the complete removal of the polymer and sintering of the Ni particles. Then, the carbon precursor methane (25 sccm) and acetonitrile (anhydrous) (20 sccm) as a nitrogen dopant were introduced in the CVD reactor and ran for 5 min, followed by rapid cooling in a mixture of hydrogen and argon at a cooling rate of 100 °C/min. The synthesized N3DG graphene sample with the nickel particles in it was then treated with 3 M HCl at 80 °C for ten hrs. to remove the metal catalyst. Finally, the sample was rinsed with ethanol and DI water and dried at room temperature for a day to obtain N3DG.

2.3. Functionalization of N3DG by Atmospheric Oxygen Plasma

The N3DG was subjected to oxygen plasma functionalization. The functionalization was conducted on a sample of dimensions (20 × 20 × 0.3 mm) by a cylindrical plasma

torch (Surfx Atom Flo 400 system, maximum RF power 200W + 3%, Redondo, CA, USA). The plasma gases used were oxygen and helium. Trials were conducted with varying the plasma parameters such as (1) plasma power and (2) oxygen flow. A stable plasma discharge was achieved by specific minimum oxygen and helium flow, set for the respective power values. Table 1 details the variation of the plasma parameter used for optimizing the N3DG functionalization. The helium gas flow rate was kept constant at 30 L/min and the plasma exposure duration was 60 s during all the trials.

Table 1. Atmospheric pressure oxygen plasma functionalizing parameters employed to nitrogen-doped graphene samples.

Sample Name	Power (W)	Oxygen (L/min)
O-N3DG_a	80	0.2
O-N3DG_b	100	0.3
O-N3DG_c	120	0.5

2.4. Coin Cell Fabrication

The symmetric supercapacitor device was fabricated as a CR2032 coin cell in an argon-filled glove box. Three types of coin cell supercapacitors were made as working electrodes: pristine three-dimensional graphene (P3DG), N-doped three-dimensional graphene (N3DG), and oxygen plasma-functionalized three-dimensional graphene (ON3DG). These electrodes were cut into 8 mm diameter discs (thickness 0.3 mm) and assembled inside the coin cell. The 3D graphene-based working electrode served as the active material and current collector in this device. The ionic electrolyte $EMIMBF_4$, about 40 µL, was used in each cell with a polypropylene microporous separator (Celgard 2400) between the electrodes. Coin cells with ON3DG and aqueous Na_2SO_4 electrolytes were also fabricated and compared with the $EMIMBF_4$ devices for electrochemical performance.

2.5. Characterization and Measurements

The surface morphology of graphene was obtained through scanning electron microscopy (FEI SCIOS dual beam 5 kV). Renishaw, in Via instrument, collected the Raman spectra of the graphene using a 514 nm Ar-ion laser with a laser spot size = 1 μm^2. The contact angle measurement was performed by a Kruss DSA100 instrument to assess the surface wettability. X-ray Photoelectron Spectroscopy (XPS) was conducted using a V.G. Thermo-Scientific MultiLab 3000 ultra-high vacuum surface analysis system, with approximately 10^{-9} Torr base pressure using an Al Kα electron source excitation energy. The Brunauer–Emmett–Teller (BET) method was employed to assess the specific surface area and pore volumes of outgassed samples by nitrogen adsorption at −196.1 °C on a Micromeritics ASAP2060 accelerated surface area and porosity measurement system. The mass of the electrodes was precisely measured by a Sartorius micro-analytical balance model ME5 with microgram resolution. Electrochemical measurements such as cyclic voltammetry, galvanostatic charge–discharge (GCD), and electrochemical impedance spectroscopy (EIS) were conducted with a workstation (Gamry, Interface 1000). EIS measurements were recorded from 10^5 to 10^{-1} Hz applying a sinusoidal voltage amplitude of 10 mV at the open circuit potential. A CT3001A1U BTS (battery test system, Vestal, NY, USA) was used to determine the cyclic stability by conducting GCD cycles.

The capacitance of the symmetric supercapacitor was calculated from the GCD curves using the equation:

$$\text{Device capacitance } C_{\text{device}},\ Cd = I\Delta t/\Delta V \tag{1}$$

$$\text{Gravimetric capacitance } C_m = C_{device}/m. \tag{2}$$

$$\text{Gravimetric energy density } Em = \frac{1}{2} * \frac{Cm(\Delta V)^2}{3.6} \tag{3}$$

$$\text{Gravimetric power density } Pm = 3600\frac{Em}{t} \tag{4}$$

where I is the discharge current, t is the discharge time, ΔV is the working voltage window, and m is the device's mass.

For non-linear GCDs,

$$\text{Gravimetric capacitance } \quad Cm = \frac{I}{m}\int 1/V(t).dt. \tag{5}$$

where I is the applied constant current density, t is the discharge time, and $V(t)$ is the potential as a function of t.

$$\text{Gravimetric energy density, } \quad Eg = 1/m\int_0^{td} iV.dt \tag{6}$$

$$\text{Average gravimetric power density, } Pg = \frac{Eg}{td} \tag{7}$$

where m is the total mass of the device, I is the discharge current, V is the potential, and td is the discharge time [5,29,32,33].

3. Results and Discussion

3.1. Morphological Characterization of N-Doped Graphene

The morphology and surface topographical images of P3DG and N3DG are displayed in Figure 1.

The SEM images of P3DG (Figure 1a,c,e) exhibit a "fluffy" morphology without many defined and dense pores. However, the images of N3DG (Figure 1b,d,f) show a highly dense, interconnected, curved 3D porous structure. The well-connected pores of the doped graphene are expected to act as good channels for ion electrolyte transport during electrochemical reactions. This hierarchical porous structure shows high flexibility combined with mechanical integrity. The porous morphology also minimizes the restacking of graphene sheets and promotes enhanced electrolyte infiltration into the graphene sheets. The surface morphology differences between N-doped and pristine graphene could cause a difference in Fermi energy, which in turn can result in modifications of the surface reactions [34]. Additionally, as mentioned before, N-doping in graphene creates more active sites in the graphene lattice, thus shifting the Fermi level above the Dirac point. The latter results in increasing charge storage and transfer [35]. These theoretical considerations seem to be proven by the CV and GCD experimental data obtained from N3DG and P3DG, as described in the next section.

3.2. Electrochemical Characterization of N-Doped Graphene

Electrochemical tests using a three-electrode cell in a 1M Na_2SO_4 solution were conducted by employing N3DG as a working electrode, Ag/AgCl as a reference electrode, and Pt wire as a counter electrode. The electrode design and the test setup are given in Supplementary Materials the Figure S1a,b of supplementary information. Similar tests were performed with P3DG as a working electrode. The obtained results are displayed in Figure 2. Figure 2a exhibits the cyclic voltammograms of P3DG and N3DG at a scan rate of 200 mV/s, where the N3DG shows an increased capacitive area by 65% when compared to P3DG. The specific capacitance calculated from the GCD curves of N3DG and P3DG, as shown in Figure S2a,b of the Supplementary Information, is in line with the above conclusion. N3DG revealed an impressive five time increase in the specific capacitance compared with the pristine 3D graphene at a current density of 1 A/g. This rise in capacitance can be attributed to the increase in numerous active sites created by the introduced nitrogen atoms onto the graphene lattice capable of attracting the electrolyte ions. Figure 2b displays the cyclic voltammogram of N3DG from a lower scan rate of 10 mV/s to a higher scan rate of 1 V/s. Rectangular CV profile is maintained at all scan rates

without any sign of Faradaic reaction, which implies that the charge storage mechanism is by surface reactions.This super-capacitive behavior involves ion adsorption/desorption at the electrode–electrolyte interface, which is not diffusion-controlled [2]. Even at the highest tested scan rate of 1000 mV/s, the CV profile remained undistorted, which confirmed a high-rate capability [36].

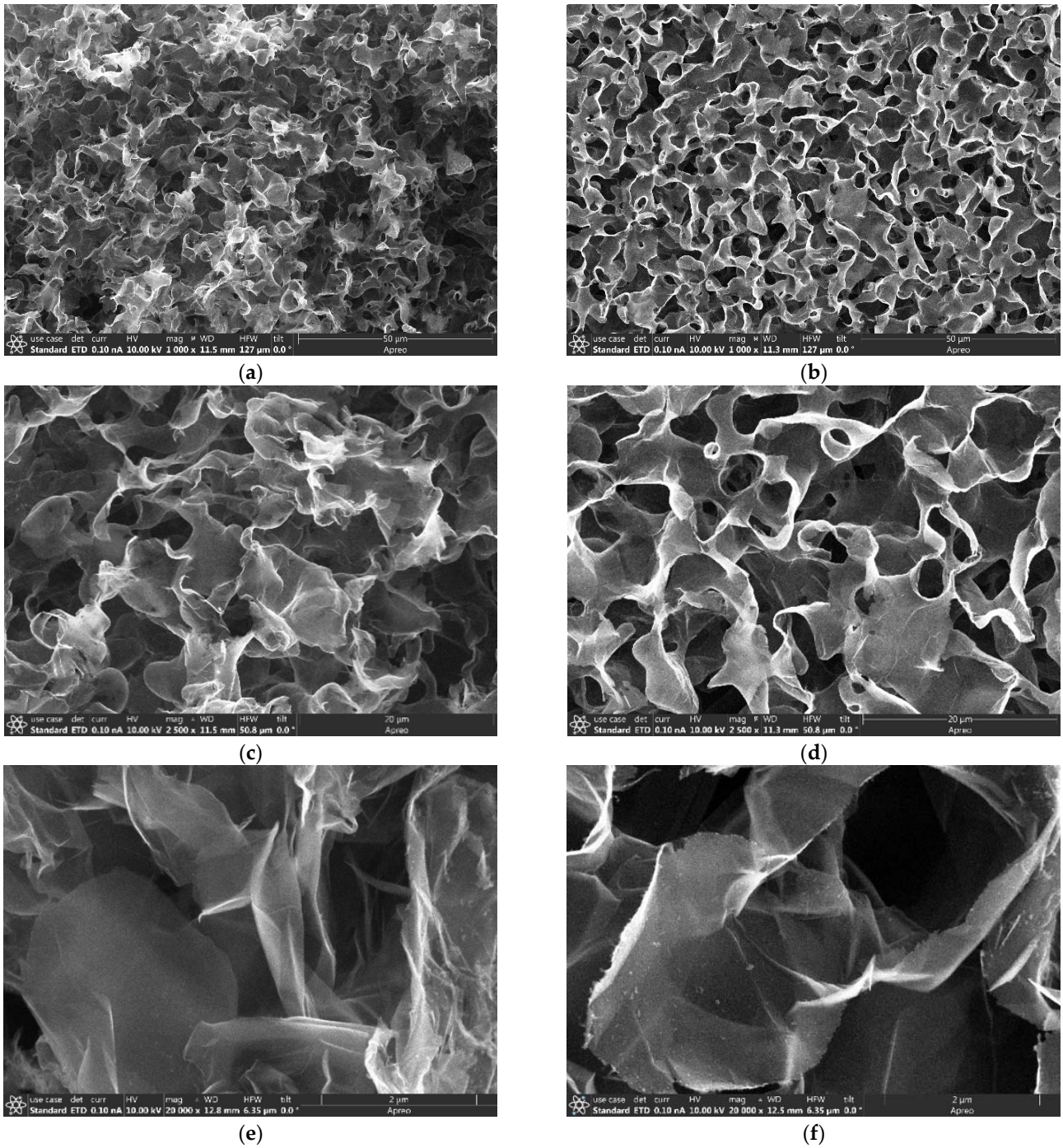

Figure 1. SEM images at different magnifications of P3DG-(**a**,**c**,**e**) and N3DG-(**b**,**d**,**f**).

Figure 2c presents the comparative Nyquist plots of N3DG and P3DG. Both the real and imaginary impedance data of pristine and N-doped graphene have been studied and plotted at frequencies from 100 kHz to 0.1 Hz. The plot consists primarily of three regions: (a) High-frequency region, where the EDLC acts purely as a resistance called

Equivalent Series Resistance (ESR). It represents the total internal resistance contributed by the electrolyte ions, the contact resistance at the interface, and the intrinsic resistance of the carbon components. (b) In the medium-frequency Nyquist plot region, both the imaginary and the real part increase. In this region, as the frequency is lowered, both the capacitance and the resistance increase; thus, the effect of electrode porosity/thickness on the ion transport between the electrode and electrolyte can be observed. (c) In the final region of the Nyquist plot, where the frequency is much lower, the imaginary part increases. Additionally, both the capacitance and resistance reach a maximum value, and the Nyquist plot is presented as a straight line [5]. Figure 2c shows that both P3DG and N3DG have an ESR of 17 and 14 Ohms, respectively, with a short 45° line followed by a 90° transition line parallel to the Y axis. The lower the ESR, the smaller the stored energy dissipation, and the higher the power performance and energy efficiency. Additionally, when the 45° line is short and followed by a vertical line, it could be interpreted as proof that all the reactive sites are fully accessible in a short time leading to capacitive behavior [33].

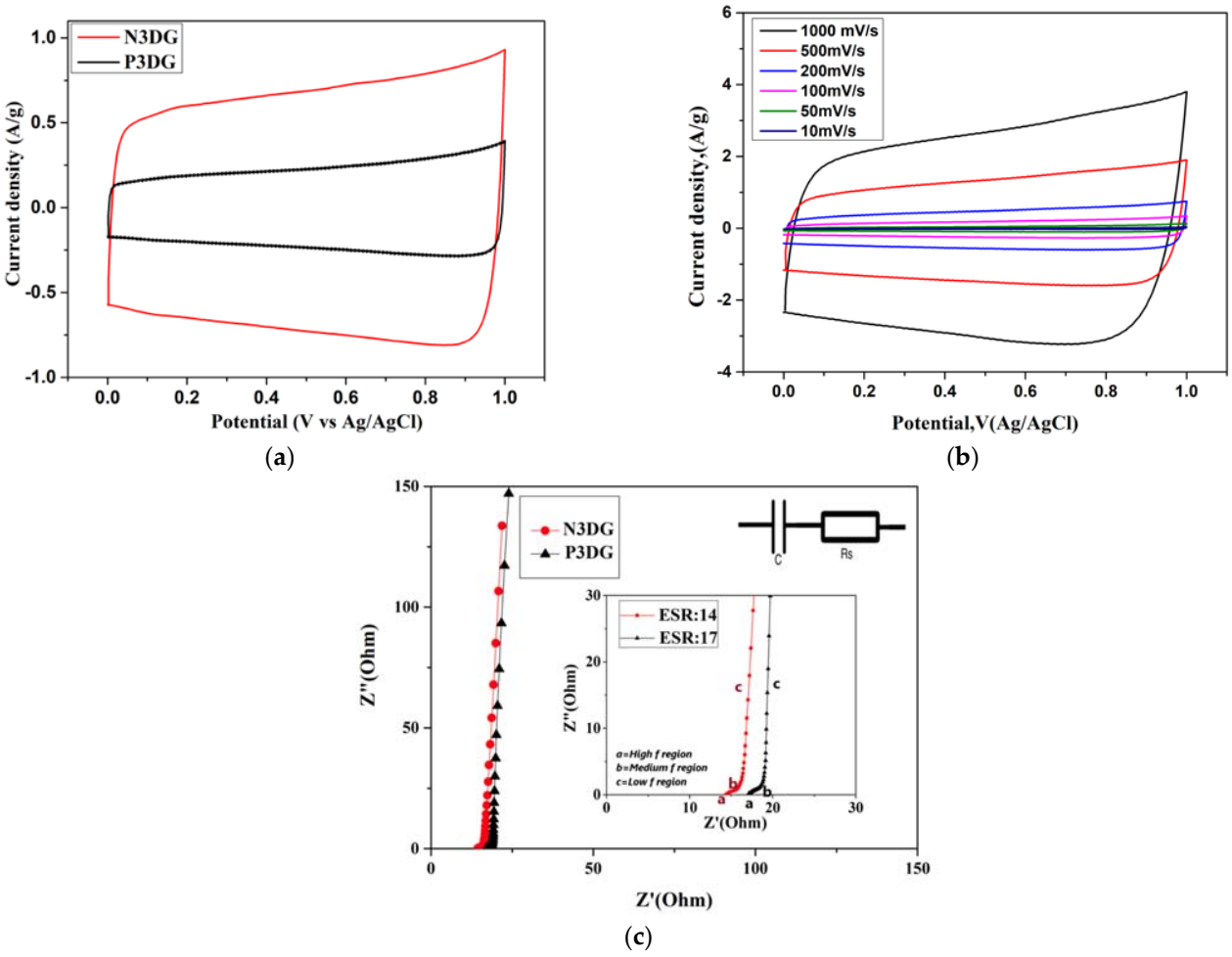

Figure 2. (**a**) Cyclic voltammetry at a scanning rate of 200 mV/s for pristine 3D graphene and N-doped 3D graphene. (**b**) Cyclic voltammetry of N3DG at scan rates varying from 10 mV/s to 1000 mV/s. (**c**) Nyquist plot for P3DG and N3DG. The inset depicts the three primary regions in the Nyquist plots for P3DG and N3DG with the related ESR values.

3.3. Optimization and Characterization of Oxygen Plasma-Functionalized N-3DG (ON3DG)

The hydrophilicity/wettability of P3DG and N3DG was assessed by contact-angle measurements. The obtained contact angle for pristine graphene was 107.3°, whereas, for N-doped graphene, it was 74.78° (Figure S3a,b from the Supplementary Information). Pristine

graphene is naturally hydrophobic due to the presence of SP^2 hybridized graphitic carbon and is comparatively less hydrophilic than N-doped graphene. Generally, a substance is called hydrophobic if the measured contact angle on its surface is greater than 90° [37]. Additionally, the hydrophilicity of N-doped graphene can be further increased to enhance its capacitive performance. Plasma functionalization is a proven technique for increasing the wettability of carbonaceous materials [27,38,39]. The N-doped graphene was functionalized using varying plasma power and oxygen flow, as detailed in Section 2.3 Table 1.

The functionalized graphene was evaluated for hydrophilicity by contact angle measurements followed by CV tests, as the EDL capacitance is directly dependent on the wettability of the electrode [40]. It was found through this study that the wettability increases with the plasma power and amount of oxygen flow. The lowest wettability is for ON3DG-a (80 W_0.2 L/m) with a contact angle of 52.18° (Figure 3a), followed by ON3DG-b (100 W_0.3 L/m) with a contact angle of 48.73° (Figure 3b). The greatest wettability was achieved for ON3DG-c (120 W_0.5 L/m) showing the lowest contact angle of 9.63° (Figure 3c).

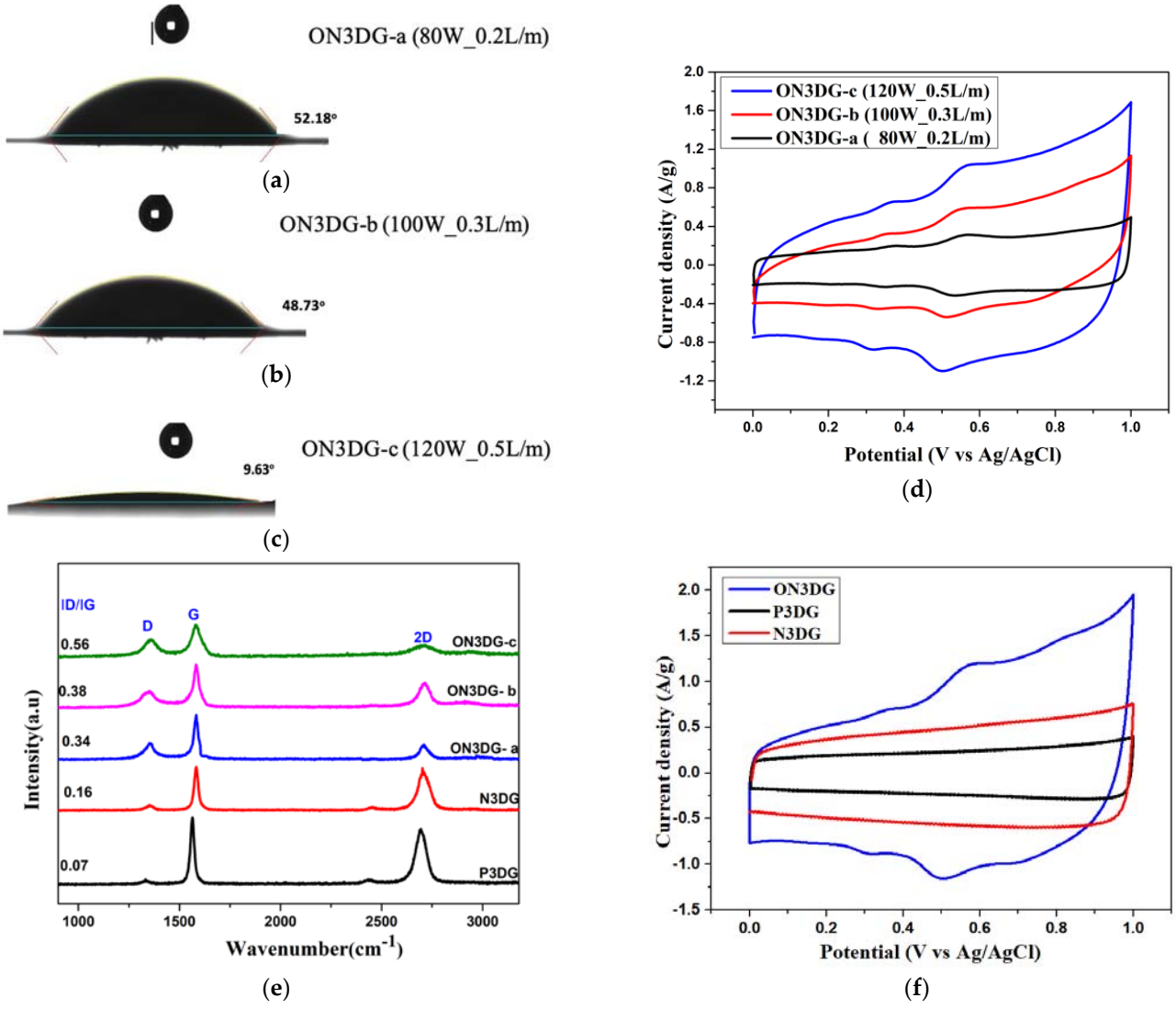

Figure 3. (**a**–**c**) Contact angle of ON3DG at different levels of plasma power. (**d**) CV curves of ON3DG obtained at different plasma powers and a scanning rate of 200 mV/s. (**e**) Raman spectra of P3DG, N3DG, and the three samples of ON3DG functionalized at different plasma power. (**f**) CV plots of ON3DG/120 W, N3DG, and P3DG at a scanning rate of 200 mV/s.

The electrochemical characteristics of the oxygen plasma functionalized graphene ON3DG with three levels of plasma power (a, b, and c) were further investigated by cyclic voltammetry using a three-electrode test cell using 1 M Na_2SO_4 electrolyte with Ag/AgCl as reference electrode and Pt as a counter electrode Figure 3d. The obtained results supported the contact angle data, showing that ON3DG/120 W, with the lowest contact angle and the highest wettability, revealed the largest area enclosed by the CV curve, followed by ON3DG/100 W. The smallest voltametric area was for ON3DG/80 W, which had the lowest wettability. There was a 25% increase in specific capacitance from ON3DG/80 W to ON3DG/100 W and a 52% increase in specific capacitance from ON3DG/100 W to ON3DG/120 W. The larger capacitance of ON3DG/120 W owes to its highest hydrophilicity, which reduces the electrode surface's ionic resistance, thus enhancing the infiltration of the aqueous electrolyte irrespective of the porosity [40]. The slight hump seen in the CV curves of all ON3DG graphene samples between 0.4 and 0.6 V could be due to the Faradaic reactions between the electrolyte and the oxygen functional groups (C=O/C-O/O-C=O), the presence of which was confirmed by the XPS results shown in Section 3.5.

Figure 3e presents the Raman spectra of pristine graphene, N-doped graphene, and the oxygen-functionalized graphene achieved with three plasma power levels. Raman spectroscopy is a reliable characterization technique that provides information about the material's quality, the presence of defects, and the number of graphene layers. It primarily yields three bands for graphene called D, G, and 2D. The G band at 1560 cm^{-1} is due to the vibration of SP^2 hybridized 'C' atoms on the same plane and indicates the graphitic band in symmetry. The 2D peak at 2690 cm^{-1} is caused by double resonant Raman scattering of the second order. The D peak at 1350 cm^{-1} implies defect-rich graphene, and the defect density can be calculated from the ratio of the intensity of D–G peaks. The higher the ratio, the greater the defect density [41–43]. From Figure 3e, we observe that the ratio increases from P3DG to ON3DG/120 W. Pristine graphene has the lowest I_D/I_G ratio value, indicating a highly ordered graphitic structure. This could be primarily due to the synthesis conditions, including a higher reaction temperature and shorter reaction time (1050 °C and 10 min, respectively) [44]. In N3DG, doping induces defects in graphene; however, there is no dramatic increase, probably due to the ordered graphitic structure and limited doping effect.

A clear D peak for all the oxygen plasma functionalized graphene has also been observed, with ON3DG/120 W/0.5 $Lm^{-1}O_2$ having the highest ID/IG value, followed by ON3DG/100 W/0.3 $Lm^{-1}O_2$. The D peak trend in ON3DG/80 W, 100 W, and 120 W shows that the functionalization, a post-synthesis treatment, induces defects proportional to the plasma power and oxygen flow. The higher the plasma power, the higher the disorder. The defects in graphene are instrumental in increasing the active surface area and sites, thus enhancing the electrochemical performance. It is also interesting to notice that the intensity of the 2D peak decreases with increasing ID/IG ratios. Several references reported similar observations of decreasing in 2D band intensity, which was proportional to the degree of disorder. When the disorder is substantially high, the 2D peak might be reduced to a bump, as observed for ON3DG/120 W [44].

ON3DG/120 W gives superior capacitive performance among the oxygen-functionalized graphene due to the highest plasma power and oxygen flow (120 W and 0.5 L/m). However, further increasing the plasma power and oxygen flow might harm the graphene structure, affecting the ion transport within the graphene layers because harsher plasma treatment conditions are detrimental [28,29]. From now, the ON3DG/120 W, optimized sample, will be referred here as ON3DG.

Figure 3f displays comparative CV plots of P3DG, N3DG, and ON3DG conducted in a three-electrode cell with a 1 M Na_2SO_4 electrolyte using Ag/AgCl as the reference electrode and Pt as a counter electrode. The CV curves show that the ON3DG encloses the largest voltammetric area, followed by N3DG and P3DG. The calculated specific capacitance based on these plots confirmed the above observation. There is a 60% increase in specific capacitance after the oxygen plasma functionalization of N-doped graphene and a 208% increase

in capacitance comparing pristine with oxygen-functionalized graphene. This impressive improvement can be attributed to the positive effects of plasma functionalization, which caused an increase in the surface functional groups, electrical conductivity, enhancement of the pore structure, and surface area [45].

3.4. Structural Characterization of ON3DG

The surface area of both P3DG and ON3DG was determined by BET. The functionalized graphene exhibits a greater surface area of 157 m^2/g when compared to the pristine graphene (41 m^2/g). This is in line with the electrochemical test results of ON3DG possessing a higher capacitance value compared to the pristine sample. Capacitance is directly proportional to the surface area for all electrochemical capacitors as per the equation $C = S\varepsilon/d$ where C is the capacitance, S is the surface area of the electrode, ε is the relative permittivity, and d is the thickness of the double-layer [4].

The porosity of graphene was characterized by nitrogen adsorption–desorption as part of the BET measurements. Figure 4a shows the comparative physisorption isotherms of ON3DG and P3DG. Both materials exhibit Type IV isotherm with a characteristic hysteresis loop for ON3DG. This loop is in the low-to-mid-range region of the relative pressure (P/P_0), indicating a comparatively large portion of mesopores [37]. The capillary condensation step of ON3DG occurs at a low relative pressure of (0.4–0.8) which corroborates with the narrow pore size distribution of mesopores with an average value of 6 nm, as seen in Figure 4b. The pore size distribution was determined by the Barret–Joyner–Halenda (BJH) method which gives a peak for ON3DG at 6 nm. In contrast, a relatively low-intensity peak for P3DG can be seen at 16 nm in Figure 4b.

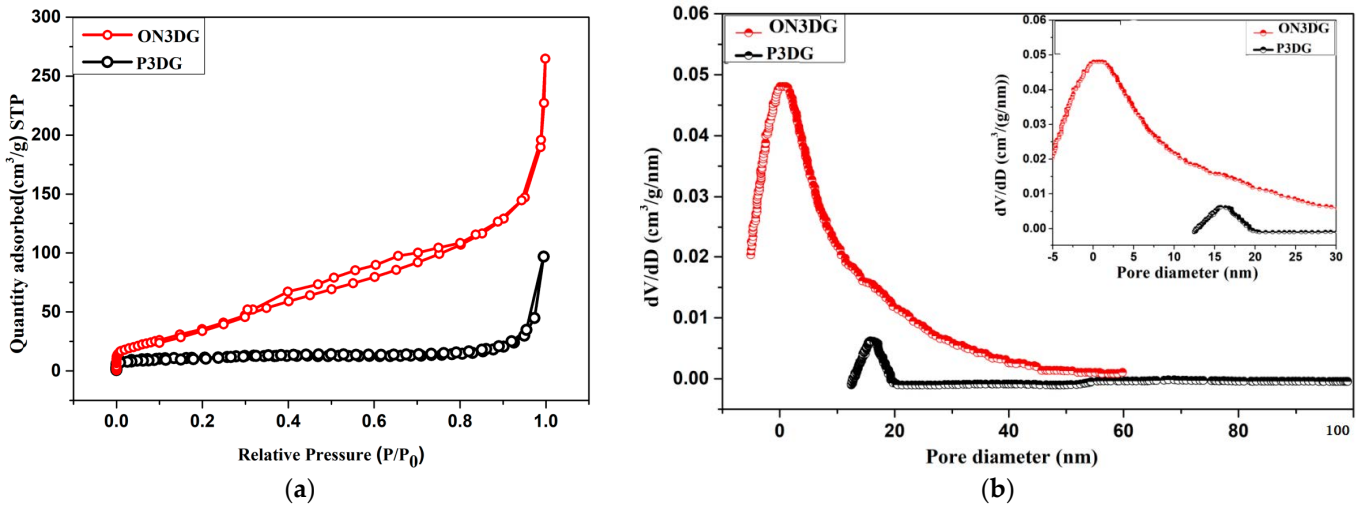

Figure 4. (**a**) N_2 adsorption–desorption isotherms. (**b**) Pore size distributions of P3DG and ON3DG. The inset in Figure 4b shows the enlarged pore size distributions (up to 30 nm) of P3DG and ON3DG.

The plot in Figure 4b indicates that during the functionalization of N-doped graphene, the mesopore region of pristine graphene was preserved; however, new pores were generated in the micropore region. The pores of P3DG were distributed between both mesopores and macro-porous regions. The total pore volume in pristine graphene is 0.135 cm^3/g, whereas, in ON3DG, it is 0.3 cm^3/g. ON3DG consists of well-defined micro and mesopores. Such a pore distribution in the functionalized graphene is highly desired for a supercapacitor because the presence of micropores provides a greater surface area supporting ion adsorption. In addition, the presence of mesopores facilitates faster ion diffusion because of a decreased ion diffusion distance from the outer electrode surface to the inner micropores. This also improves the rate capability of the supercapacitor [8,46,47].

3.5. Chemical Characterization of ON3DG

X-ray photoelectron spectroscopy (XPS) was conducted on the pristine and functionalized graphene to investigate the elemental compositions and confirm the type of the functional groups. Figure 5a presents the survey spectra of the pristine, N-doped, and functionalized N-doped graphene. The total carbon content decreases from P3DG (98.5%) to N3DG (89.37%), and ON3DG (85.98).

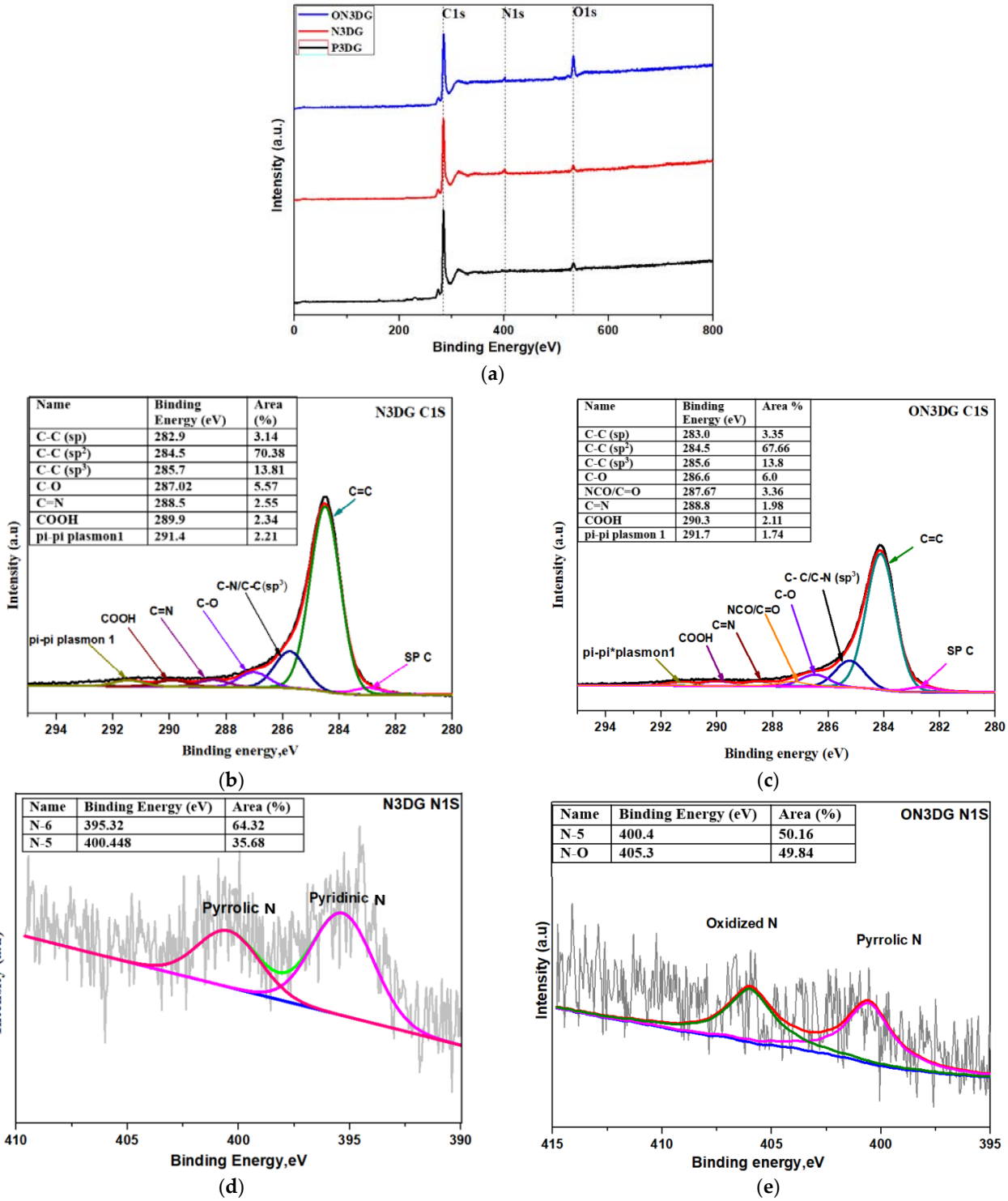

Figure 5. *Cont.*

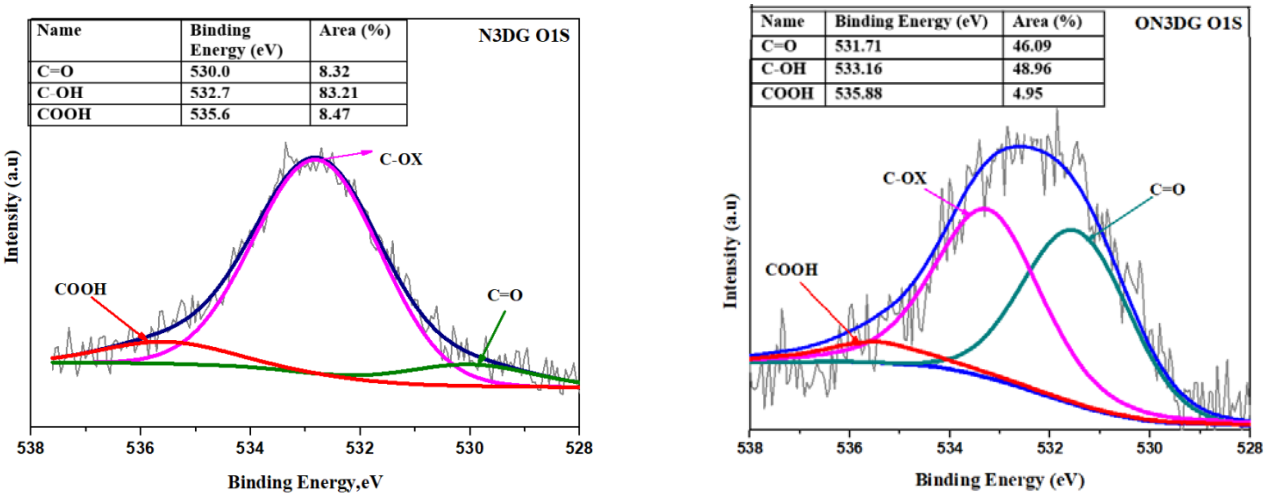

Figure 5. (**a**) Survey spectrum of P3DG, N3DG, and ON3DG. (**b**,**c**) C1s (carbon) spectrum of N3DG and ON3DG. (**d**,**e**) N1s (nitrogen) spectrum of N3DG and ON3DG. (**f**,**g**) O1s (oxygen) spectrum of N3DG and ON3DG. The elemental XPS spectra are deconvoluted to reveal the functional groups and chemical bonding.

Table 2 displays the elemental composition of P3DG, N3DG, and ON3DG based on the XPS results. The elemental composition of P3DG was retrieved from the data reported earlier by our group [28]. Figure 5b–g presents a detailed quantification of the functional groups found in the C1s, N1s, and O1s of N3DG and ON3DG.

Table 2. Elemental composition of P3DG, N3DG, and ON3DG based on the XPS results.

Element (%)	**Samples**		
	P3DG	N3DG	ON3DG
Carbon (C1s)	98.5	89.37	85.98
Oxygen (O1s)	1.5	8.63	12.42
Nitrogen (N1s)	-	2.0	1.6

The XPS peak deconvolution was performed using Shirley-type baseline and Lorentzian (20%)/Gaussian functions. Figure 5b,c reveal the (C1s) deconvolution spectra of the N3DG and ON3DG samples. The binding energy at 284.5 eV corresponds to the graphitic carbon with sp^2 hybridization. The binding energy at 285.6 eV can be related to the C–H/C–N bond from the defective carbon in the hexagonal lattice, which is sp^3 hybridized, while the band at 283 eV denotes sp carbon. At the tail end of the C1s, one can find that the ether/alcohol group (C-OH~286.6 eV), C=N group (~288 eV), carboxyl group (COOH~289.9), and pi–pi plasmon at 291–292 eV. The oxygen-functionalized graphene has an extra peak at 287.6 eV pertaining to the O=C-N bond, which is not seen for non-functionalized graphene [48]. Additionally, the percentage of graphitic carbon C=C and C=N is less in ON3DG when compared to N3DG.

Deconvoluting the high-resolution N1s spectra Figure 5d,e obtained from N3DG reveals two types of nitrogen, namely pyridinic (N-6) at 395.3 eV and pyrrolic nitrogen (N-5) at 400.4 eV. In ON3DG samples, pyrrolic nitrogen was found at 400.4 eV, and oxidized nitrogen species were identified at 405.3 eV (NO^{-}, -C-NO_2, and C-ONO) which replaced the pyridinic nitrogen found in N3DG [49]. The pyrrolic N-5 and pyridinic N-6 nitrogen are usually located at the edge of the graphene layers and are considered responsible for the pseudocapacitive effect. Pyridinic-type nitrogen is sp^2 hybridized to two carbon atoms and donates one pi electron to the aromatic system. The pyrrolic nitrogen is a five-

member ring bonded to the adjacent carbon atoms from the phenolic/carbonyl groups and donates two pi electrons. In contrast, oxidized N species actively affect electron transfer through the lattice due to their positive charge, thus enhancing conductivity rather than capacitance [49].

High-resolution O1s spectra are presented in Figure 5 f,g. The band at 532.5 ± 1.0 eV representing the hydroxyl group (OH) bonded to C, prominent in both N3DG and ON3DG, is followed by the bands for carbonyl group C=O at ~530. 5 ± 1.0 eV and carboxyl group COOH at ~534.5 ± 1.0 eV [8,50,51].

3.6. Electrochemical Characterization of a Symmetrical Supercapacitor Device

Full cell devices based on P3DG, N3DG, and ON3DG were fabricated as coin cell supercapacitors with 8 mm diameter discs. Individual devices were made of each type of graphene as symmetrical electrodes and separated by Celgard 2400 grade polypropylene, immersed in 40 µL EMIMBF4 ionic electrolyte. The graphene discs were designed as free-standing electrodes; hence, metallic current collectors were not needed, making the device much lighter than conventional cells. The graphene discs functioned simultaneously as the device's current collectors and active materials. The fabricated coin cells were subjected to various electrochemical measurements. The cyclic voltammograms in Figure 6a present a comparative study of P3DG, N3DG, and ON3DG at a scan rate of 1 V/s. All three CV geometries revealed a non-Faradaic geometry, thus confirming that the prominent charge storage mechanism is capacitive. Comparing the CV loop areas of the three graphene materials studied here, the largest area was obtained from ON3DG, followed by N3DG, and finally, P3DG. ON3DG exhibits an area 52% greater than N3DG and 77% greater than P3DG. The higher capacitance for ON3DG can be due to the comparatively higher surface area and the pseudo capacitance resulting from both the nitrogen and oxygen functional groups. Figure 6b displays the voltammograms of ON3DG at different scan rates from 25 mV/s to 1 V/s. Even at a very high scan rate of 1 V/s, the device preserved its CV profile showing good super-capacitive behaviors.

The CV profile, especially of ON3DG in Figure 6a, is oblique, unlike the perfectly rectangular profile of the three electrode CV curves for P3DG and N3DG obtained with an aqueous electrolyte, as shown earlier in Section 3.2. This is because of the larger resistance offered by the organic electrolyte and the presence of hydroxyl and carbonyl redox groups [52,53]. A study by Sillars et al. [54] explained the cause of the obliqueness of the CV curve in ON3DG, which is more visible above 2.5 V. As per this work, the possible explanation could be the decomposition of electrolytes such as $EMIMBF_4$ below the determined electrochemical stability window (ESW). This could happen when the electrolyte accesses a greater percentage of the graphene surface area resulting in its non-uniform charging. The latter leads to a higher charge at some surface spots, causing the voltage to exceed the ESW, resulting in the steep rise in the current in the obtained voltammograms [54].

The electrochemical impedance spectroscopy (EIS) measurement was also conducted on the supercapacitors from 10^{-1} to 10^{5} Hertz frequency. The Nyquist plots in Figure 6c display EIS spectra of typical EDLCs with a small semicircle in the high-frequency region and straight lines with two different slopes in the medium and low-frequency range. Detailed Nyquist plot interpretation was presented earlier in Section 3.2. The ESR or equivalent series resistance for ON3DG, N3DG, and P3DG was obtained as 2.0,1.7, and 1.3 Ohms, respectively. As mentioned earlier, since the ESR is very low for all three supercapacitor devices, the energy dissipation is also lower, resulting in higher power performance and energy efficiency. Additionally, the short lines with 45° slopes followed by vertical lines imply that all the reactive sites are fully accessible in a short time leading to a capacitive behavior.

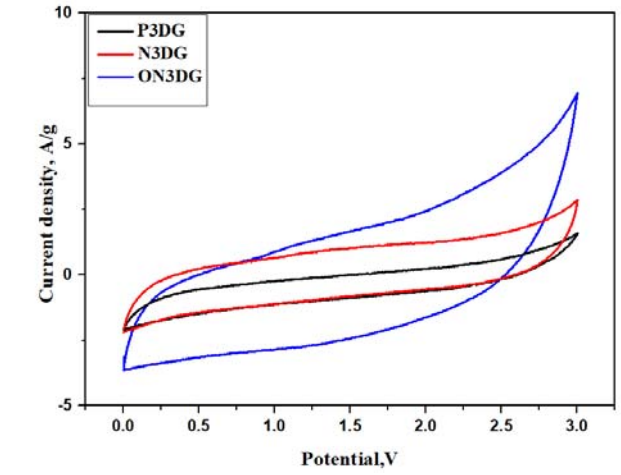

(**a**)

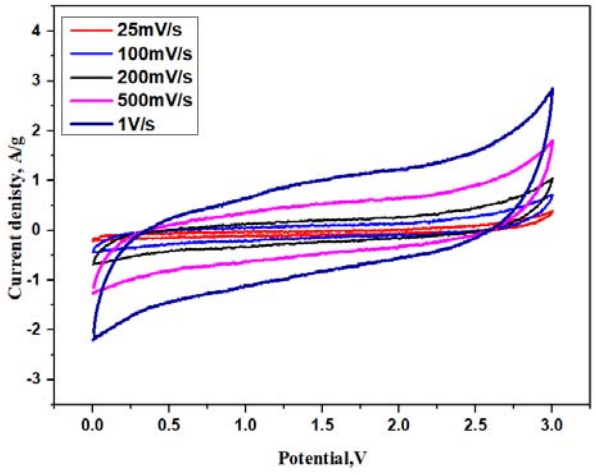

(**b**)

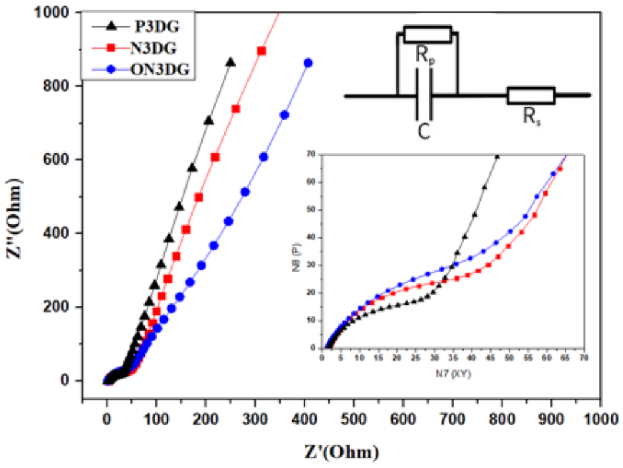

(**c**)

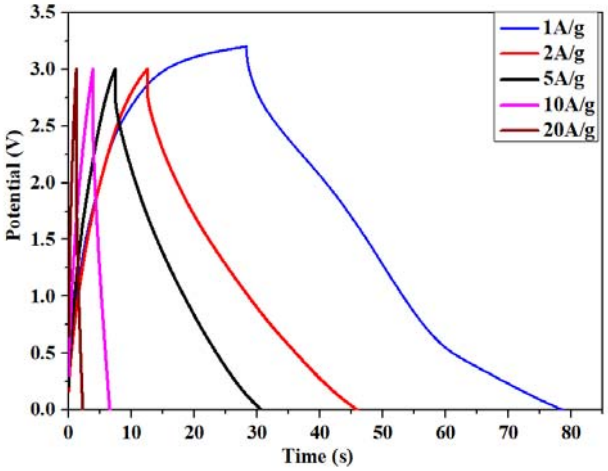

(**d**)

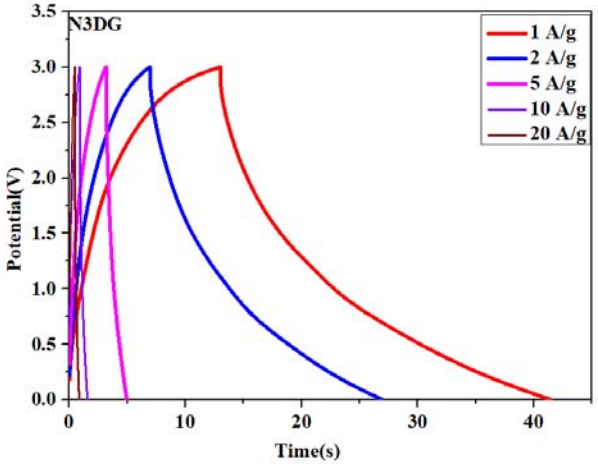

(**e**)

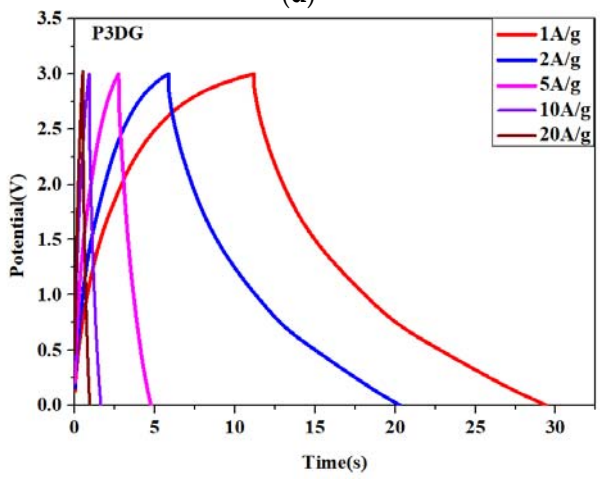

(**f**)

Figure 6. *Cont.*

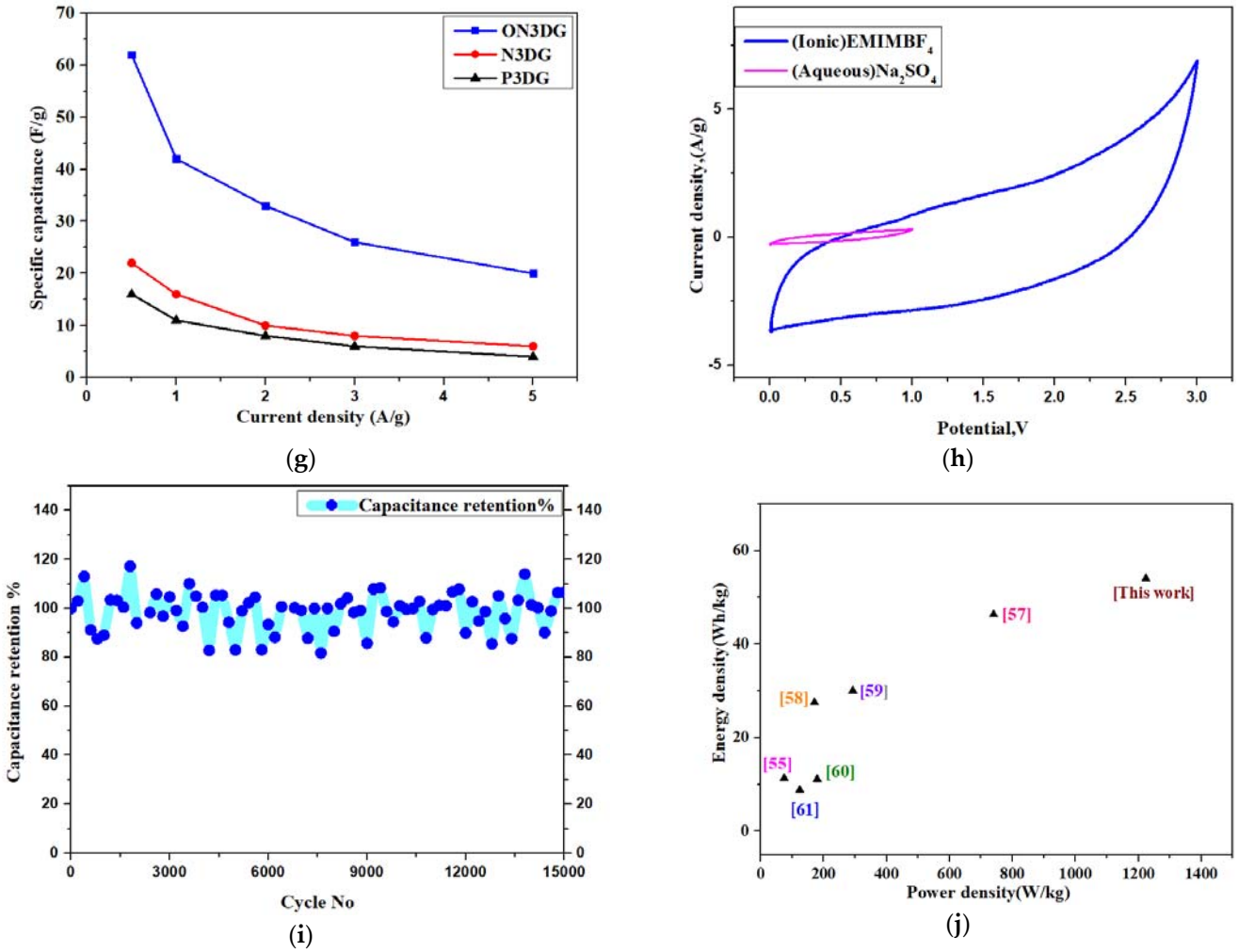

Figure 6. (**a**,**c**) Comparative CV and EIS plots of P3DG, N3DG, and ON3DG, respectively. The inset in 6c reveals the high-frequency region with low ESRs. (**b**) CV of ON3DG obtained at different scan rates. (**d**–**f**) GCD curves of P3DG, N3DG, and ON3DG, respectively. (**g**) Specific capacitance vs. current density of P3DG, N3DG, and ON3DG. (**h**) Comparative CV curves of ON3DG device in aqueous (Na_2SO_4 and ionic ($EMIMBF_4$) electrolytes. (**i**) Cyclic stability of ON3DG. (**j**) Ragone plot comparing the current work (ON3DG device) with recent similar studies in the public domain.

Galvanostatic charge–discharge was conducted on the coin cell devices to better understand their electrochemical behavior. Figure 6d–f reveal the GCD plots of ON3DG, P3DG, and N3DG, respectively. The GCD profile for all three devices shows a slight deviation from the linear, triangular behavior. This deviation can be ascribed to the Faradaic reactions between the surface oxygen functional groups and the organic electrolyte [52,53]. The specific capacitance at 0.5 A/g current density is given by 62 F/g for ON3DG, 22 F/g for N3DG, and 16 F/g for P3DG. This trend shows that nitrogen doping improves the capacitance by 25%, and further functionalization with oxygen plasma increases the capacitance by 64.5%. Thus, the high specific capacitance of ON3DG can be attributed to the following reasons. (1) A comparatively larger surface area with an effective contribution of micro/mesopores facilitating ion adsorption and quick ion/charge transport. (2) Increased electronic conductivity because of the doped nitrogen groups. (3) Improved wettability and pseudocapacitive effects due to the presence of oxygen functional groups. Since the electrode is highly porous with an unmeasurable surface area, gravimetric capacitance is used instead of aerial/volumetric capacitance. The total mass of the two electrodes in the coin cell device used in the calculations is 0.46 mg. The energy density and power density

were calculated as 54 Wh/kg and a power density of 1224 W/kg at a current density of 0.5 A/g. The energy and power densities are superior to other similar recently published doped graphene-based supercapacitor works (Table S1).

Figure 6g presents the rate capability of the three device types tested at a current density from 0.5 A/g to 5 A/g. The specific capacitance of ON3DG remained at 58% at a higher current density of 2 A/g, whereas for N3DG and P3DG, it stayed at 45% and 43%, respectively. This could be due to the higher mesopore volume in ON3DG, which shortened the ion diffusion distance, thus facilitating faster charge transport. At higher current densities, a drop in discharge voltage, called I.R. drop, was noticed in all three supercapacitors, which proportionately increased with the current densities. At current densities greater than 5 A/g, capacitance values for all three device types seem to decrease. This is caused by the low ion mobility, which slows their transfer to the pore walls from the bulk to form a double layer when the current rate increases [1].

Figure 6h displays the comparative CV plots of ON3DG in aqueous Na_2SO_4 and ionic $EMIMBF_4$ electrolytes. The CV loop area of the Na_2SO_4 device is much smaller (>86%) than that of the $EMIMBF_4$ device. Additionally, the energy and power density of the $EMIMBF_4$ device is undoubtedly superior to those of the Na_2SO_4 primarily because of the significant difference in the voltage windows provided by these two electrolytes (aqueous of 1 V vs. ionic of 3 V).

The durability of the high-performing ON3DG device was assessed by GCD cycles at a current density of 1 A/g, and the result of this test is shown in Figure 6i. The device demonstrated impressive capacitance retention of 107% after 15,000 cycles. The initial few hundred cycles showed a diminished specific capacitance, after which it stabilized beyond the 1000th cycle and remained steady within 100% capacitance retention until the highest cycle number. The percentage of capacitance retention slightly fluctuated above and below 100% throughout the 15,000 cycles but never went below 80%. The varying capacitance retention observed might be due to the changing pseudo capacitance caused by the oxygen functional groups and pore structure modification during cycling.

The diminished capacitance may be caused by the unstable oxygen functional groups (triggering pseudo capacitance) either via their transformation or elimination. For example, the unstable carboxylic group could be changed to C=O/C-O, then to the C-H group, resulting in a decrease in oxygen content during cycling. The superior capacitance retention could be due to an electro-activation phenomenon. This includes the motion of graphene sheets to adjust to different ion sizes of the electrolyte. Longer charge–discharge cycles also help ions intercalate between the graphene sheets, creating more surface area, which produces additional double-layer charging, resulting in higher capacitance [52]. Additionally, access to the available micropores would be limited during the initial cycling stages. Subsequently, the increase in the electrode's wettability and the electronegativity of the oxygen functional groups, would facilitate the ion entry into the micropores, enhancing further deeper penetration, thus improving the pore utilization to the maximum. As a result, double-layer charging and pseudo-capacitance will be facilitated with an increase in charge–discharge cycles. All this helped increase the capacitance, further stabilizing and yielding high performance cycles [1,55].

The cyclic stability of graphene with oxygen functional groups in an ionic electrolyte is notable despite the fact that at higher current rates, the reversibility is reduced, and the performance is also reduced due to the interaction between oxygen functional groups and ionic electrolytes. Moreover, the oxygen functional groups are reported to have the discredit of increasing the internal resistance of carbon, especially the bulkier -COOH group, which is proven to disrupt the EDL (electric double layer), and thus reduce the non-Faradaic capacitance. However, in this work, the formation of the -COOH group is suppressed by hydroxyl/ether/quinone carbon groups (as evident from XPS data), which could be a prominent factor for the observed higher cyclic stability [56].

Figure 6j shows the Ragone plot comparing the current work with recent similar studies. The comparison is based on Supplementary Materials Table S1 in the Supplementary Information, which presents the literature data on the electrochemical performance of different heteroatom-doped carbon-based electrodes in two-electrode systems based on recent publications from the public domain [55,57–61]. This table reveals the superiority of this work with respect to energy and power densities compared to other similar works on symmetric supercapacitors fabricated from heteroatom-doped carbon/graphene electrodes.

4. Conclusions and Future Perspective

A symmetric supercapacitor based on nitrogen-doped and oxygen-functionalized graphene electrodes was successfully fabricated. The obtained significant energy and power density of 54 Wh/kg and 1224 W/kg at a current density of 0.5 A/g, combined with cyclic stability of 15,000 cycles, were enabled, thanks to the following strategies. (a) Synthesizing a porous and well-graphitized 3D graphene structure, which contributed to double-layer capacitance; (b) inducing pseudo-capacitance by incorporating nitrogen and oxygen functional groups via CVD doping and atmospheric pressure plasma treatment, respectively; and (c) the usage of lowly viscous and highly conductive ionic electrolyte with a wide voltage window. The approaches described here can be successfully employed to fabricate high-performing commercial supercapacitors in the future. For future perspectives, the ionic electrolyte EMIMBF4 with PVDF-HFP as gel polymer electrolyte can be successfully used in fabricating next-generation high-performance nanocarbon-based, wearable supercapacitors.

Supplementary Materials: The supporting information can be downloaded at: https://www.mdpi.com/article/10.3390/batteries8120258/s1, Figure S1: (a) Picture of the electrode used in the 3 electrode test-(a), Three electrode test set up-(b); Figure S2: GCD curves at different current densities of pristine-(a) and N-doped 3D graphene–(b)in three-electrode set up with Ag/AgCl as reference electrode, Pt as counter electrode in a 1M sodium sulfate aqueous electrolyte; Figure S3: Contact angle measurement of pristine-(a), N-doped 3D graphene-(b); Table S1: Electrochemical performance of different carbon-based electrodes in two electrode systems based on recent publications found in the public domain.

Author Contributions: Conceptualization, K.M.J.; Formal analysis, K.M.J.; Funding acquisition, V.S.; Investigation, K.M.J.; Methodology, K.M.J.; Project administration, K.M.J.; Resources, V.S.; Supervision, V.S.; Validation, K.M.J.; Writing – original draft, K.M.J.; Writing – review & editing, V.S. All authors have read and agreed to the published version of the manuscript.

Funding: This research was funded by NSF through grant # 2016484 and by PRP pilot grant at the University of Cincinnati # 1016487.

Data Availability Statement: Not applicable.

Conflicts of Interest: The authors declare no conflict of interest.

References

1. Sillars, F.B.; Fletcher, S.I.; Mirzaeian, M.; Hall, P.J. Effect of activated carbon xerogel pore size on the capacitance performance of ionic liquid electrolytes. *Energy Environ. Sci.* **2010**, *4*, 695–706. [CrossRef]
2. Wang, Y.; Song, Y.; Xia, Y. Electrochemical capacitors: Mechanism, materials, systems, characterization and applications. *Chem. Soc. Rev.* **2016**, *45*, 5925–5950. [CrossRef] [PubMed]
3. Kumar, Y.; Rawal, S.; Joshi, B.; Hashmi, S.A. Background, fundamental understanding and progress in electrochemical capacitors. *J. Solid State Electrochem.* **2019**, *23*, 667–692. [CrossRef]
4. Frackowiak, E.; Beguin, F. Carbon materials for the electrochemical storage of energy in capacitors. *Carbon* **2001**, *39*, 937–950. [CrossRef]
5. Noori, A.; El-Kady, M.F.; Rahmanifar, M.S.; Kaner, R.B.; Mousavi, M.F. Towards establishing standard performance metrics for batteries, supercapacitors and beyond. *Chem. Soc. Rev.* **2019**, *48*, 1272–1341. [CrossRef] [PubMed]
6. Li, J.; Hu, Y.; Xie, H.; Peng, J.; Fan, L.; Zhou, J.; Lu, B. Weak cation–solvent interactions in ether-based electrolytes stabilizing potassium-ion batteries. *Angew. Chem.* **2022**, *134*, e202208291.
7. Hu, Y.; Fan, L.; Rao, A.M.; Yu, W.; Zhuoma, C.; Feng, Y.; Qin, Z.; Zhou, J.; Lu, B. Cyclic-anion salt for high-voltage stable potassium metal batteries. *Natl. Sci. Rev.* **2022**, *9*, nwac134. [CrossRef] [PubMed]

8. Wu, Y.; Cao, J.-P.; Zhuang, Q.-Q.; Zhao, X.-Y.; Zhou, Z.; Wei, Y.-L.; Zhao, M.; Bai, H.-C. Biomass-derived three-dimensional hierarchical porous carbon network for symmetric supercapacitors with ultra-high energy density in ionic liquid electrolyte. *Electrochim. Acta* **2021**, *371*, 137825. [CrossRef]
9. Chen, S.; Qiu, L.; Cheng, H.-M. Carbon-Based Fibers for Advanced Electrochemical Energy Storage Devices. *Chem. Rev.* **2020**, *120*, 2811–2878. [CrossRef] [PubMed]
10. Miao, L.; Song, Z.; Zhu, D.; Li, L.; Gan, L.; Liu, M. Ionic Liquids for Supercapacitive Energy Storage: A Mini-Review. *Energy Fuels* **2021**, *35*, 8443–8455. [CrossRef]
11. Lai, F.; Feng, J.; Yan, R.; Wang, G.-C.; Antonietti, M.; Oschatz, M. Breaking the Limits of Ionic Liquid-Based Supercapacitors: Mesoporous Carbon Electrodes Functionalized with Manganese Oxide Nanosplotches for Dense, Stable, and Wide-Temperature Energy Storage. *Adv. Funct. Mater.* **2018**, *28*, 1801298. [CrossRef]
12. Kwon, H.-N.; Jang, S.-J.; Kang, Y.C.; Roh, K.C. The effect of ILs as co-salts in electrolytes for high voltage supercapacitors. *Sci. Rep.* **2019**, *9*, 1–6. [CrossRef] [PubMed]
13. Chen, Y.; Liu, Z.; Sun, L.; Lu, Z.; Zhuo, K. Nitrogen and Sulfur co-doped porous graphene aerogel as an efficient electrode material for high performance supercapacitor in ionic liquid electrolyte. *J. Power Sources* **2018**, *390*, 215–223. [CrossRef]
14. Hurilechaoketu; Wang, J.; Cui, C.; Qian, W. Highly electroconductive mesoporous activated carbon fibers and their performance in the ionic liquid-based electrical double-layer capacitors. *Carbon* **2019**, *154*, 1–6. [CrossRef]
15. Guan, J.; Rao, A.M.; Zhou, J.; Yu, X.; Lu, B. Structure-Optimized Phosphorene for Super-Stable Potassium Storage. *Adv. Funct. Mater.* **2022**, *32*, 2203522. [CrossRef]
16. Kesavan, T.; Aswathy, R.; Raj, I.A.; Kumar, P.; Ragupathy, P. Nitrogen-Doped Graphene as Electrode Material with Enhanced Energy Density for Next-Generation Supercapacitor Application. *ECS J. Solid State Sci. Technol.* **2015**, *4*, M88–M92. [CrossRef]
17. Shao, Y.; El-Kady, M.F.; Wang, L.J.; Zhang, Q.; Li, Y.; Wang, H.; Mousavi, M.F.; Kaner, R.B. Graphene-based materials for flexible supercapacitors. *Chem. Soc. Rev.* **2015**, *44*, 3639–3665. [CrossRef]
18. Huang, Y.; Liang, J.; Chen, Y. An Overview of the Applications of Graphene-Based Materials in Supercapacitors. *Small* **2012**, *8*, 1805–1834. [CrossRef] [PubMed]
19. Zhang, Q.; Cheng, X.; Wang, C.; Rao, A.M.; Lu, B. Sulfur-assisted large-scale synthesis of graphene microspheres for superior potassium-ion batteries. *Energy Environ. Sci.* **2020**, *14*, 965–974. [CrossRef]
20. Kondapalli, V.K.R.; He, X.; Khosravifar, M.; Khodabakhsh, S.; Collins, B.; Yarmolenko, S.; Puente, A.P.Y.; Shanov, V. CVD Synthesis of 3D-Shaped 3D Graphene Using a 3D-Printed Nickel–PLGA Catalyst Precursor. *ACS Omega* **2021**, *6*, 29009–29021. [CrossRef]
21. Shao, Y.; Zhang, S.; Engelhard, M.H.; Li, G.; Shao, G.; Wang, Y.; Liu, J.; Aksay, I.A.; Lin, Y. Nitrogen-doped graphene and its electrochemical applications. *J. Mater. Chem.* **2010**, *20*, 7491–7496. [CrossRef]
22. Wei, D.; Liu, Y.; Wang, Y.; Zhang, H.; Huang, L.; Yu, G. Synthesis of N-Doped Graphene by Chemical Vapor Deposition and Its Electrical Properties. *Nano Lett.* **2009**, *9*, 1752–1758. [CrossRef] [PubMed]
23. Inagaki, M.; Toyoda, M.; Soneda, Y.; Morishita, T. Nitrogen-doped carbon materials. *Carbon* **2018**, *132*, 104–140. [CrossRef]
24. Lee, W.J.; Maiti, U.N.; Lee, J.M.; Lim, J.; Han, T.H.; Kim, S.O. Nitrogen-doped carbon nanotubes and graphene composite structures for energy and catalytic applications. *Chem. Commun.* **2014**, *50*, 6818–6830. [CrossRef] [PubMed]
25. Savilov, S.; Arkhipova, E.; Ivanov, A.; Maslakov, K.; Shen, Z.; Aldoshin, S.; Lunin, V. Pyrolytic synthesis and characterization of N-doped carbon nanoflakes for electrochemical applications. *Mater. Res. Bull.* **2015**, *69*, 7–12. [CrossRef]
26. Joseph, K.M.; Kasparian, H.J.; Shanov, V. Carbon Nanotube Fiber-Based Wearable Supercapacitors—A Review on Recent Advances. *Energies* **2022**, *15*, 6506. [CrossRef]
27. Malik, R.; McConnell, C.; Alvarez, N.T.; Haase, M.; Gbordzoe, S.; Shanov, V. Rapid, in situ plasma functionalization of carbon nanotubes for improved CNT/epoxy composites. *RSC Adv.* **2016**, *6*, 108840–108850. [CrossRef]
28. Zhang, L.; DeArmond, D.; Alvarez, N.T.; Malik, R.; Oslin, N.; McConnell, C.; Adusei, P.K.; Hsieh, Y.; Shanov, V. Flexible Micro-Supercapacitor Based on Graphene with 3D Structure. *Small* **2017**, *13*, 1603114. [CrossRef]
29. Adusei, P.K.; Gbordzoe, S.; Kanakaraj, S.N.; Hsieh, Y.-Y.; Alvarez, N.T.; Fang, Y.; Johnson, K.; McConnell, C.; Shanov, V. Fabrication and study of supercapacitor electrodes based on oxygen plasma functionalized carbon nanotube fibers. *J. Energy Chem.* **2019**, *40*, 120–131. [CrossRef]
30. DeArmond, D.; Zhang, L.; Malik, R.; Reddy, K.V.K.; Alvarez, N.T.; Haase, M.R.; Hsieh, Y.-Y.; Kanakaraj, S.N.; Oslin, N.; Brunemann, J.; et al. Scalable CVD synthesis of three-dimensional graphene from cast catalyst. *Mater. Sci. Eng. B* **2020**, *254*, 114510. [CrossRef]
31. Reddy, A.L.M.; Srivastava, A.; Gowda, S.R.; Gullapalli, H.; Dubey, M.; Ajayan, P.M. Synthesis of Nitrogen-Doped Graphene Films for Lithium Battery Application. *ACS Nano* **2010**, *4*, 6337–6342. [CrossRef] [PubMed]
32. Owusu, K.A.; Qu, L.; Li, J.; Wang, Z.; Zhao, K.; Yang, C.; Hercule, K.M.; Lin, C.; Shi, C.; Wei, Q.; et al. Low-crystalline iron oxide hydroxide nanoparticle anode for high-performance supercapacitors. *Nat. Commun.* **2017**, *8*, 14264. [CrossRef] [PubMed]
33. Mathis, T.S.; Kurra, N.; Wang, X.; Pinto, D.; Simon, P.; Gogotsi, Y. Energy Storage Data Reporting in Perspective—Guidelines for Interpreting the Performance of Electrochemical Energy Storage Systems. *Adv. Energy Mater.* **2019**, *9*, 1902007. [CrossRef]
34. Tavkhelidze, A.; Bibilashvili, A.; Jangidze, L.; Gorji, N. Fermi-Level Tuning of G-Doped Layers. *Nanomaterials* **2021**, *11*, 505. [CrossRef] [PubMed]
35. Wang, X.; Ding, Y.; Chen, F.; Lu, H.; Zhang, N.; Ma, M. Hierarchical Porous N-doped Graphene Monoliths for Flexible Solid-State Supercapacitors with Excellent Cycle Stability. *ACS Appl. Energy Mater.* **2018**, *1*, 5024–5032. [CrossRef]

36. Wang, M.; Ma, Y. Nitrogen-doped graphene forests as electrodes for high-performance wearable supercapacitors. *Electrochim. Acta* **2017**, *250*, 320–326. [CrossRef]
37. Beguin, F.; Frackowiak, E.; Gogotsi, Y. *Carbons for Electrochemical Energy Storage and Conversion Systems*; CRC Press: Boca Raton, FL, USA, 2009.
38. Dulyaseree, P.; Yordsri, V.; Wongwiriyapan, W. Effects of microwave and oxygen plasma treatments on capacitive characteristics of supercapacitor based on multiwalled carbon nanotubes. *Jpn. J. Appl. Phys.* **2016**, *55*, 02BD05. [CrossRef]
39. Meng, J.; Nie, W.; Zhang, K.; Xu, F.; Ding, X.; Wang, S.; Qiu, Y. Enhancing Electrochemical Performance of Graphene Fiber-Based Supercapacitors by Plasma Treatment. *ACS Appl. Mater. Interfaces* **2018**, *10*, 13652–13659. [CrossRef] [PubMed]
40. Deheryan, S.; Cott, D.J.; Mertens, P.W.; Heyns, M.; Vereecken, P. Direct correlation between the measured electrochemical capacitance, wettability and surface functional groups of CarbonNanosheets. *Electrochim. Acta* **2014**, *132*, 574–582. [CrossRef]
41. Bokobza, L.; Bruneel, J.-L.; Couzi, M. Raman Spectra of Carbon-Based Materials (from Graphite to Carbon Black) and of Some Silicone Composites. *C J. Carbon Res.* **2015**, *1*, 77–94. [CrossRef]
42. Lavin-Lopez, M.P.; Valverde, J.L.; Cuevas, M.C.; Garrido, A.; Sanchez-Silva, L.; Martinez, P.; Romero-Izquierdo, A. Synthesis and characterization of graphene: Influence of synthesis variables. *Phys. Chem. Chem. Phys.* **2013**, *16*, 2962–2970. [CrossRef] [PubMed]
43. Claramunt, S.; Varea, A.; López-Díaz, D.; Velázquez, M.M.; Cornet, A.; Cirera, A. The Importance of Interbands on the Interpretation of the Raman Spectrum of Graphene Oxide. *J. Phys. Chem. C* **2015**, *119*, 10123–10129. [CrossRef]
44. Ferreira, E.; Moutinho, M.V.O.; Stavale, F.; Lucchese, M.M.; Capaz, R.B.; Achete, C.A.; Jorio, A. Evolution of the Raman spectra from single-, few-, and many-layer graphene with increasing disorder. *Phys. Rev. B* **2010**, *82*, 125429. [CrossRef]
45. Conway, B.E. *Electrochemical Supercapacitors: Scientific Fundamentals and Technical Applications*; Kluwer Academic/Plenum: New York, NY, USA, 1999.
46. Wang, G.; Zhang, J.; Kuang, S.; Zhou, J.; Xing, W.; Zhuo, S. Nitrogen-doped hierarchical porous carbon as an efficient electrode material for supercapacitors. *Electrochim. Acta* **2015**, *153*, 273–279. [CrossRef]
47. Li, J.-G.; Ho, Y.-F.; Ahmed, M.M.M.; Liang, H.-C.; Kuo, S.-W. Mesoporous Carbons Templated by PEO-PCL Block Copolymers as Electrode Materials for Supercapacitors. *Chem. A Eur. J.* **2019**, *25*, 10456–10463. [CrossRef]
48. Steffen, T.T.; Fontana, L.C.; Nahorny, J.; Becker, D. Role of nitrogen–oxygen plasma functionalization of carbon nanotubes in epoxy nanocomposites. *Polym. Compos.* **2018**, *40*, E1162–E1171. [CrossRef]
49. Chernyak, S.A.; Ivanov, A.S.; Arkhipova, E.A.; Shumyantsev, A.V.; Strokova, N.E.; Maslakov, K.I.; Savilov, S.V.; Lunin, V.V. Mechanism and kinetics of decomposition of N-containing functional groups in few-layer graphene nanoflakes. *Appl. Surf. Sci.* **2019**, *484*, 228–236. [CrossRef]
50. Zhang, R.; Jing, X.; Chu, Y.; Wang, L.; Kang, W.; Wei, D.; Li, H.; Xiong, S. Nitrogen/oxygen co-doped monolithic carbon electrodes derived from melamine foam for high-performance supercapacitors. *J. Mater. Chem. A* **2018**, *6*, 17730–17739. [CrossRef]
51. Krüner, B.; Schreiber, A.; Tolosa, A.; Quade, A.; Badaczewski, F.; Pfaff, T.; Smarsly, B.M.; Presser, V. Nitrogen-containing novolac-derived carbon beads as electrode material for supercapacitors. *Carbon* **2018**, *132*, 220–231. [CrossRef]
52. Cheng, Q.; Tang, J.; Ma, J.; Zhang, H.; Shinya, N.; Qin, L.-C. Graphene and carbon nanotube composite electrodes for supercapacitors with ultra-high energy density. *Phys. Chem. Chem. Phys.* **2011**, *13*, 17615–17624. [CrossRef] [PubMed]
53. Okhay, O.; Tkach, A. Graphene/Reduced Graphene Oxide-Carbon Nanotubes Composite Electrodes: From Capacitive to Battery-Type Behaviour. *Nanomaterials* **2021**, *11*, 1240. [CrossRef]
54. Sillars, F.B.; Fletcher, S.I.; Mirzaeian, M.; Hall, P.J. Variation of electrochemical capacitor performance with room temperature ionic liquid electrolyte viscosity and ion size. *Phys. Chem. Chem. Phys.* **2012**, *14*, 6094–6100. [CrossRef]
55. Fan, S.; Wei, L.; Liu, X.; Ma, W.; Lou, C.; Wang, J.; Zhang, Y. High-density oxygen-enriched graphene hydrogels for symmetric supercapacitors with ultrahigh gravimetric and volumetric performance. *Int. J. Hydrogen Energy* **2021**, *46*, 39969–39982. [CrossRef]
56. Jerigová, M.; Odziomek, M.; López-Salas, N. "We Are Here!" Oxygen Functional Groups in Carbons for Electrochemical Applications. *ACS Omega* **2022**, *7*, 11544–11554. [CrossRef] [PubMed]
57. Arkhipova, E.A.; Ivanov, A.S.; Maslakov, K.I.; Savilov, S.V. Nitrogen-doped mesoporous graphene nanoflakes for high performance ionic liquid supercapacitors. *Electrochim. Acta* **2020**, 353. [CrossRef]
58. Kwon, S.H.; Lee, E.; Kim, B.S.; Kim, S.G.; Lee, B.J.; Kim, M.S.; Jung, J.C. Activated carbon aerogel as electrode material for coin-type EDLC cell in organic electrolyte. *Curr. Appl. Phys.* **2014**, *14*, 603–607. [CrossRef]
59. Balaji, S.S.; Raj, A.G.; Karnan, M.; Sathish, M. Investigations on the nature of electrolyte on the electrochemical supercapacitor performance of heteroatom doped graphene. *Ionics (Kiel)* **2020**, *26*, 2081–2094. [CrossRef]
60. Kim, S.J.; Son, Y.J.; Jeon, B.; Han, Y.S.; Kim, Y.J.; Jung, K.H. Surface crosslinking of 6FDA-durene nanofibers for porous carbon nanofiber electrodes in electrochemical double layer capacitors. *Nanotechnology* **2020**, *31*, 215404. [CrossRef]
61. Zhang, Y.; Fan, S.; Li, S.; Song, Y.; Wen, G. 3D porous oxygen-enriched graphene hydrogels with well-balanced volumetric and gravimetric performance for symmetric supercapacitors. *J. Mater. Sci.* **2020**, *55*, 12214–12231. [CrossRef]